

Three-Dimensional Nanostructured Air Electrode for Sodium–Oxygen Batteries: A Mechanism Study toward the Cyclability of the Cell

Hossein Yadegari,[†] Mohammad Norouzi Banis,[†] Biwei Xiao,[†] Qian Sun,[†] Xia Li,[†] Andrew Lushington,[†] Biqiong Wang,[†] Ruying Li,[†] Tsun-Kong Sham,[‡] Xiaoyu Cui,[§] and Xueliang Sun^{*,†}

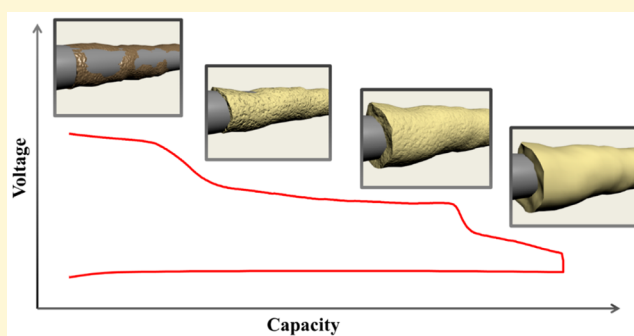
[†]Department of Mechanical and Materials Engineering, University of Western Ontario, London, Ontario N6A 5B9, Canada

[‡]Department of Chemistry, University of Western Ontario, London, Ontario N6A 5B7, Canada

[§]Canadian Light Source, Saskatoon S7N 0X4, Canada

Supporting Information

ABSTRACT: A binder-free three-dimensional (3D) nanostructured air electrode composed of vertically grown nitrogen doped carbon nanotubes on carbon paper (NCNT-CP) is developed and applied to Na–O₂ cells. The 3D architecture of the air electrode results in increased discharge capacity by optimizing the utilized area of the electrode material. The chemical and electrochemical reaction mechanisms of the cell are also explored with the use of synchrotron-based X-ray absorption spectroscopy (XAS). Investigation of the discharge product of Na–O₂ cells during discharge and charge cycles using X-ray absorption near-edge structure (XANES) indicates that both sodium superoxide and peroxide are produced under various physicochemical conditions and can be subsequently decomposed with different overpotentials. Furthermore, formation of carbonate-based parasitic products is also shown to restrict the cyclability of the cell.



INTRODUCTION

Rechargeable nonaqueous alkali metal–O₂ batteries, such as Li– and Na–O₂, have recently attracted a great amount of attention due to their high theoretical energy density.^{1–4} This high theoretical energy density is related to the use of high energy alkali metals as a negative and oxygen, from ambient air, as the positive electrode materials. The primary discharge products of these cells are typically metal oxides, which are insoluble in nonaqueous electrolytes, resulting in accumulation on the porous air electrode surface. On the basis of this, an ideal air electrode should have a porous structure with appropriate pore volume and pore size distribution in addition to necessary characteristics such as conductivity, chemical stability, high surface area, and low cost.⁵ The porous structure of the air electrode serves to increase oxygen diffusion into the positive electrode materials as well as appropriately accommodate formation and storage of the discharge product.^{5,6} Reversing the solid-state discharge products of these cells requires overcoming a relatively large charging overpotential, which is one of the major challenges facing the development of alkali metal–O₂ batteries.⁴ Formation of parasitic side products is also believed to contribute to the large overpotential required during the charge cycle.^{7,8}

Chemical composition of the discharge products may also greatly affect the charging overpotential of alkali metal–O₂ cells. It has been almost well established that the major discharge

product of the Li–O₂ cell in a relatively stable electrolyte is lithium peroxide (Li₂O₂).^{2,9–11} However, some reports indicate the presence of a lithium superoxide-like phase alongside Li₂O₂, resulting in a lower charging overpotential.^{12–15} Nevertheless, the chemical composition of discharge product in Na–O₂ cells remains still a point of controversy. Both sodium peroxide (Na₂O₂) and superoxide (NaO₂) are almost evenly identified as the major discharge products for Na–O₂ cells. Liu et al. and Li et al. identified formation of Na₂O₂ in Na–O₂ cells using an ether-based electrolyte and a charging overpotential of ~1.5 V.^{16,17} A hydrated form of sodium peroxide (Na₂O₂·2H₂O) has also been found in other studies.^{18,19} Interestingly, Hartmann et al. investigated the Na–O₂ cell in which a unique structure of cubic NaO₂ in micrometer size range was observed as the discharge product and decomposed below 2.5 V versus Na/Na⁺ (charging overpotential of ~0.2 V).^{3,20,21} Furthermore, using differential electrochemical mass spectrometry (DEMS) analysis, McCloskey et al. showed that the discharge product of Na–O₂ cells is predominantly NaO₂.²² More recently, Zhao et al. showed that NaO₂ is the main product under static oxygen atmosphere, while Na₂O₂·2H₂O was obtained under flowing oxygen gas.²³ Theoretical calculations also have been applied to

Received: February 3, 2015

Revised: April 2, 2015

Published: April 6, 2015

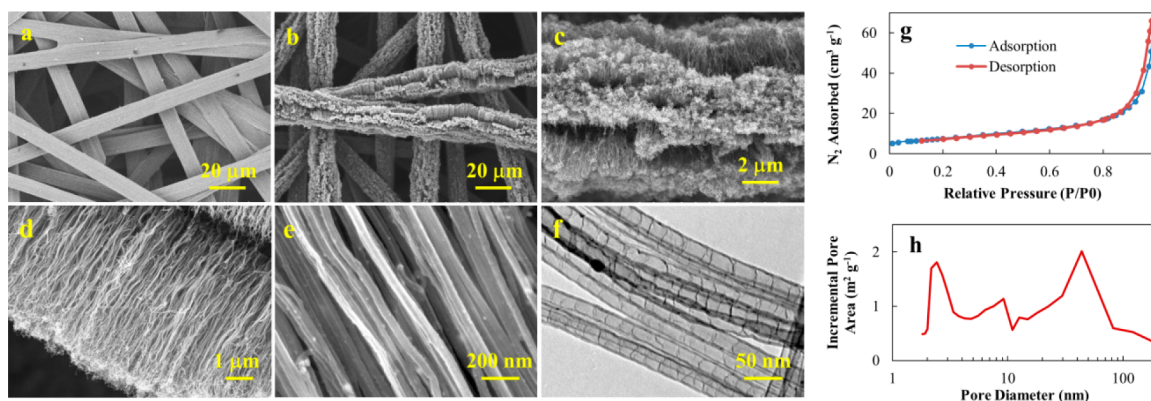


Figure 1. (a–e) SEM and (f) TEM micrographs of (a) pristine CP and (b–f) NCNT-CP air electrode synthesized via SPCVD method for 3 min; (g) nitrogen adsorption/desorption isotherm of the synthesized NCNT-CP air electrode; (h) pore size distribution plot of the NCNT-CP air electrode.

predict the discharge product of these Na–O₂ cells. NaO₂ phase was suggested by first-principle density functional theory (DFT) calculations to be stable discharge product of Na–O₂ cell under standard conditions (300 K and 1 atm).²⁴ On the other side, by combining the surface energies of various sodium oxide crystals with the energy of bulk compounds, Cedar et al. demonstrated that bulk Na₂O₂ is the more stable phase under the standard conditions and that NaO₂ is more stable at the nanoscale or under higher oxygen partial pressures.²⁵

Since various metal oxides exhibit different overpotentials during the charge cycle, manipulating the formation of the discharge products is an attractive way to control the charge overpotential of the cell. Our group has recently demonstrated that the discharge product of Na–O₂ cells is composed of both peroxide and superoxide phases. In addition, the chemical composition and consequently the charge overpotential of the Na–O₂ cell was shown to be controlled by changing the kinetic parameters of the cell.²⁶ In the present study, a high surface area binder-free air electrode with a three-dimensional (3D)-structure is developed and employed in a Na–O₂ cell. We show that the capacity of the air electrode can be significantly increased by using a 3D structured air electrode through the increasing of the electrode material utilization. Additionally, the chemical composition of Na–O₂ cell products is traced during the discharge and charge cycles of the cell with the aid of a synchrotron-based XAS technique. Meanwhile, the binder-free nature of the 3D-structured air electrode in the present study eliminates any uncertainty regarding the probable contribution from the binder decomposition in the chemical and electrochemical responses of the cell.

EXPERIMENTAL SECTION

Preparation of the Air Electrode. The NCNT-CP electrode was prepared using a spray pyrolysis chemical vapor deposition (SPCVD) method, as described elsewhere.²⁷ In a typical synthesis, a piece of carbon paper (CP) was sputtered with a 30 nm of aluminum as the buffer layer. The CP was then fixed inside a quartz tube and transferred into a vertical furnace. The quartz tube was purged with argon gas (99.999%) at a flow rate of 500 sccm for 20 min. The furnace was then heated up to 850 °C. After the temperature was fixed at 850 °C, a solution containing 2 g of imidazole and 0.2 g of ferrocene in 10 mL of acetonitrile was introduced into the tube with the aid of an ultrasonic probe sonicator at a flow rate of 250 μL/min for various times from 3–10 min (see Supporting Information for detailed synthesis process).

Physical Characterizations. Morphological studies were performed by Hitachi S-4800 field-emission scanning electron microscope (SEM) and Hitachi H-7000 transmission electron microscope (TEM) operated at 10 and 100 kV, respectively. N₂ adsorption/desorption isotherms were obtained using a Folio Micromeritics TriStar II 3020 Surface Area and Pore Size Analyzer. The surface area of the electrodes was calculated by the Brunauer, Emmett, and Teller (BET) model by taking at least six data points where 0.07 < P/P₀ < 0.2. Pore size distribution was obtained by the Barrett, Joyner, and Halenda (BJH) model using the desorption branch of the isotherm. Thermogravimetric analysis (TGA) was performed using a SDT Q600 TGA unite from room temperature (RT) to 900 °C in air at a heating rate of 10 °C min⁻¹. X-ray photoelectron spectroscopy (XPS) was carried out by a Kratos Axis Ultra Al-α spectrometer operated at 14 kV. Raman data were collected using a HORIBA Scientific LabRAM HR Raman spectrometer operated with an incident laser beam at 532.03 nm. X-ray diffractograms were obtained using a Bruker D8 Advance (Cu–Kα source, 40 kV, 40 mA). For the X-ray diffraction (XRD) measurements, the Na–O₂ cells were disassembled in the Ar-filled glovebox after testing, and the positive electrode materials were placed into an air-sensitive XRD sample holder. XAS measurements were obtained at the Canadian Light Source (CLS) on the spherical grating monochromator (SGM) beamline. The air electrodes of Na–O₂ cells were washed with the same solvent that was used for preparing the electrolyte. Afterward, the electrodes were dried and sealed inside the glovebox and then moved to the analysis place, where the samples were opened in the second glovebox and directly introduced to the XAS vacuum chamber. The samples were kept under pure argon atmosphere before the analytical measurements, without any exposure to the atmospheric air. The vacuum during the XAS experiments was around 10⁻⁸ Torr. The standard samples (Li₂O₂, 90%; Na₂O₂, >95%; KO₂, 100%; Na₂CO₃, >99.5%) were purchased from Sigma-Aldrich and analyzed as received.

Electrochemical Measurements. Swagelok-type cells composed of sodium foil anode, Celgard 3500 separator (5/8 in. in diameter), different air electrode, and a stainless steel mesh as current collector were used to carry out electrochemical measurements. The employed Swagelok cell configuration is illustrated in Figure S2. The air electrodes were cut into circular pieces (3/8 in. in diameter) with the geometric surface area of 0.71 cm². The average weight of 20 pieces of CP electrodes was measured and applied as the weight of CP substrate. The average geometric surface area and weight of the CP substrate were 0.71 cm² and 5.8 mg. The loading of NCNTs was calculated based on the TGA data to be 0.24 mg cm⁻². The whole weight of NCNT + CP or geometric surface area of the air electrode has been used for calculating the specific capacity of the NCNT-CP air electrode. A fresh sodium foil was prepared with the aid of a homemade press machine using the sodium metal stick (from Aldrich) as starting sodium metal and circular pieces (3/8 in. in diameter) inside the argon-filled glovebox. The electrolyte used in this study was

0.5 M sodium triflate (NaSO_3CF_3 , 98%, Aldrich) dissolved in diethylene glycol diethyl ether (DEGDME, reagent grade $\geq 98\%$, Aldrich). Sodium triflate electrolyte salt was dried at 80°C under vacuum for 48 h, and the water content of DEGDME solvent was removed using molecular sieves for at least 10 days. The amount of electrolyte in the cell was $\sim 200\ \mu\text{L}$. The assembled $\text{Na}-\text{O}_2$ cells were placed into a homemade testing box inside the glovebox and then transferred to the testing room. The argon content of testing box was moderately vacuumed out and then pure oxygen (purity 4.3) was purged into the box. The pressure of testing box was kept at 1.0 atm during the electrochemical tests. Discharge/charge characteristics were performed using an Arbin BT-2000 battery station at RT (25°C).

RESULTS AND DISCUSSION

The porous structure of the air electrode plays a major role in the overall performance of alkali metal- O_2 cells. This electrode must be able to allow sufficient oxygen and metal ion diffusion while simultaneously providing adequate storage for discharge products. To address these requirements, a new air electrode is developed based on the 3D structure of CP, which is covered by vertically grown NCNTs through a one-step spray pyrolysis chemical vapor deposition (SPCVD) method. NCNT grown on CP was chosen as the air electrode in this study since conjugation between the nitrogen lone-pair electrons and graphite π -system enhances the electrical conductivity and electrocatalytic activity of CNT.^{28–31} The structure of the CP substrate and NCNT-CP air electrode was observed using SEM and TEM, as shown in Figure 1. The CP substrate (Figure 1a) is composed of randomly oriented fibers with a diameter of around $10\ \mu\text{m}$, exhibiting a 3D structure with diverse micrometer sized pores. After NCNTs were grown on CP (Figure 1b–d) through a SPCVD process, a uniform layer of NCNTs with around $10\ \mu\text{m}$ in length covers the carbon fibers. The high-resolution SEM and TEM micrographs of NCNTs shown in Figure 1, panels e and f exhibit bamboo-like structure with stacked-cone structure, which is characteristic of NCNTs (see Figure S3 for more TEM images). The nitrogen adsorption/desorption isotherm of the NCNT-CP electrode material (Figure 1g) shows a mixed shape of type II (at medium pressures) and type IV (at higher pressures) according to the IUPAC classification. This result indicates the presence of both macropores (pore diameter $>50\ \text{nm}$) as well as the mesopores ($2\ \text{nm} < \text{pore diameter} < 50\ \text{nm}$). The BET surface area and total pore volume of NCNT-CP electrode was determined to be $27.3\ \text{m}^2\ \text{g}^{-1}$ and $0.106\ \text{cm}^3\ \text{g}^{-1}$, respectively. Pore size distribution plot (Figure 1h) of the NCNT-CP air electrode also confirms the presence of the macro and mesopores. This is a dual-porous structure in which large micrometer sized pores existing between the individual fibers increase volume of oxygen and sodium ions transportation, while the solid state discharge product can be captured within the mesopores space provided by the NCNTs. In addition, XPS analysis of the NCNTs (Figure S4) indicated the nitrogen content of NCNTs to be 5% (calculated based on the peak area ratio between nitrogen and carbon divided by their atomic sensitivity factors). Further, Raman spectra of the NCNT-CP air electrode (Figure S5) exhibit two main peaks around 1350 and $1590\ \text{cm}^{-1}$, which correspond to the D-band and the G-band, respectively. The D-band is originated from atomic displacement and disorder induced features caused by lattice defect or distortion, while the G-band indicates the presence of crystalline graphitic carbon. The intensity ratio of D and G bands (I_D/I_G) is used to evaluate the disorder in the materials. The I_D/I_G ratio of synthesized NCNTs was calculated to be 1,

which indicates a high amount of defects and disorder in NCNTs as a result of N-doping into the CNT structure.

The specific capacities based on both of the geometric surface area (mAh cm^{-2}) and the total weights (mAh g^{-1}) of CP and NCNT-CP electrodes obtained at a current density of $0.1\ \text{mA cm}^{-2}$ are compared in Figure 2, panel a. The NCNT-

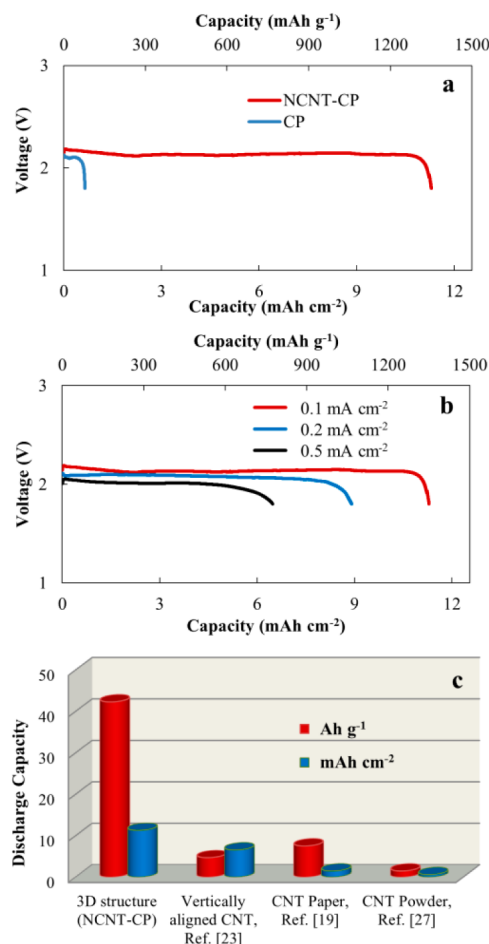


Figure 2. (a) Discharge curves of pristine CP and NCNT-CP air electrodes (NCNT length of $10\ \mu\text{m}$) at a current density of $0.1\ \text{mA cm}^{-2}$. (b) Discharge curves of NCNT-CP air electrodes obtained at different current densities of 0.1, 0.2, and $0.5\ \text{mA cm}^{-2}$. (c) The specific capacities are calculated based on the geometric surface area (mAh cm^{-2}) and also based on the total weights of CP and NCNT-CP electrodes (mAh g^{-1}); the specific capacity for NCNT-CP and other CNTs containing air electrodes with different architectures including powder-based, CNTs paper, and vertically aligned CNTs from the literature.

CP electrode exhibits a specific capacity 17 times higher than bare CP electrode. The increase in specific capacity is related to the increased surface area provided by NCNTs allowing for discharge product to form, while the micrometer sized pores of CP structure guarantee the continuous supply of oxygen and sodium ions onto the electrode surface. This 3D structure fosters a uniform coverage of discharge products on the electrode surface while maintaining sufficient respiration. The capability of the NCNT-CP air electrode to supply sufficient amounts of oxygen and sodium ions was also examined by discharging the cell under elevated current densities (Figure 2b). The specific capacity of the $\text{Na}-\text{O}_2$ cell is reduced by 1.7 times when increasing the discharge current density from 0.1 to

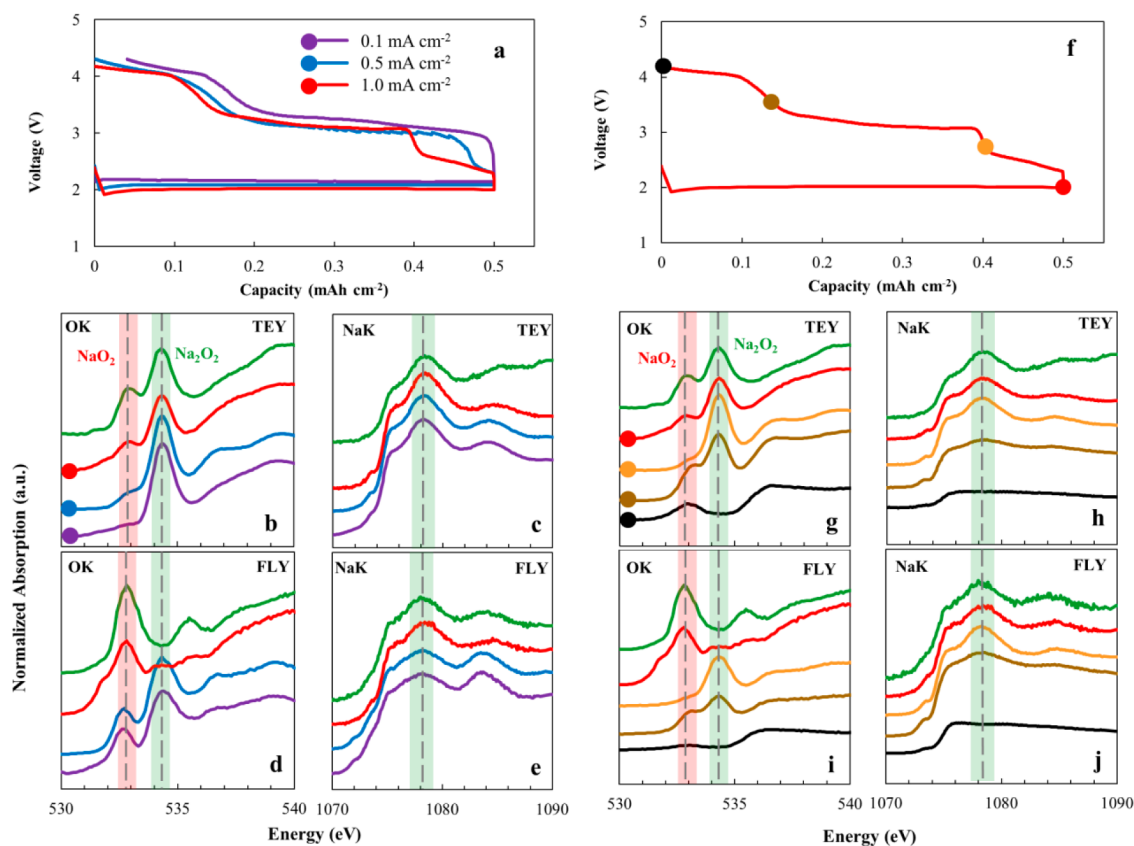


Figure 3. (a) Restricted discharge and charge curves of Na–O₂ cell using NCNT-CP air electrode recorded at different discharge current densities of 0.1, 0.5, and 1.0 mA cm⁻² and a constant charge current density of 0.1 mA cm⁻². Normalized (b,d) O and (c,e) Na K-edge XANES spectra recorded under the (b,c) TEY and (d,e) FLY modes for the NCNT-CP air electrodes discharged under different current densities of 0.1, 0.5, and 1.0 mA cm⁻² as well as standard Na₂O₂ sample; (f) restricted discharge and charge curves of Na–O₂ cell using NCNT-CP air electrode recorded at discharge and charge current density of 1.0 and 0.1 mA cm⁻², respectively. Normalized (g,i) O and (h,j) Na K-edge XANES spectra recorded under the (g,h) TEY and (i,j) FLY modes for the NCNT-CP air electrodes charged to the various cutoff potentials of 2.75, 3.5, and 4.3 V as well as the discharged air electrode and the standard Na₂O₂ sample.

0.5 mA cm⁻², which indicates the proper structure of the breathing air electrode. The discharge/charge curves of the NCNT-CP air electrode under various current densities and full discharge depth are also shown in Figure S6.

It should also be noted that the majority of weight for the NCNT-CP air electrode stems from the underlying CP substrate. The weight percentage of NCNTs was calculated based on TGA and determined to comprise only 3% of the overall weight (Figure S7). Replacing the CP substrate with a more lightweight material may further increase both specific gravimetric capacity and rate capability of the cell. Recalculation of the specific capacity of NCNT-CP air electrode (after subtraction of 80 mAh g⁻¹ for CP) based on only the weight of NCNTs results in an incredible value of 42.29 Ah g_{NCNTs}⁻¹, which illustrates the increased utilization of NCNTs in the 3D air electrode architecture.

In Figure 2, panel c, the specific capacity of NCNT-CP air electrode is compared with corresponding values from literature for other CNTs containing air electrodes with alternate architectures including powder-based electrode, CNT paper, and vertically aligned CNTs.^{19,23,32} In all cases, the air electrodes are discharged under a current density of 0.1 mA cm⁻², while the specific capacity is calculated based on either the electrodes geometric surface area or the weight of CNTs and NCNTs. The obtained specific capacity of the NCNT-CP air electrode is significantly higher than that of other reported

air electrodes. Discharge curves for NCNT-CP air electrodes prepared with longer NCNTs displays similar discharge curves, as shown in Figure S8. However, electrodes with longer NCNTs of 15 and 25 μm show lower discharge capacities compared to electrodes with 10 μm long NCNTs. Furthermore, increasing the discharge current density for electrodes prepared with longer NCNTs resulted in larger capacity drops as a result of decreased macropore volume (see also Figure S9).

Recently, we showed that the chemical composition, and consequently the charge overpotential of the Na–O₂ cell, may be altered via modifying kinetic parameters such as discharge current density.²⁶ Figure 3, panel a shows the electrochemical response of Na–O₂ cells discharged to a restricted capacity of 0.5 mAh cm⁻² at various current densities from 0.1–1.0 mA cm⁻² and subsequently charged back using a constant current density of 0.1 mA cm⁻². Two charge plateaus beginning at 2.9 and 4.0 V can be seen for cells discharged at a low current density of 0.1 mA cm⁻². For cells discharged at an increased current density of 0.5 mA cm⁻², the charge cycle exhibits a small plateau at 2.3 V, and then the charge potential increases to 2.9 and 4.0 V, forming the second and third plateaus. In the case of Na–O₂ cell discharged at a high current density of 1.0 mA cm⁻², three clearly distinct charge plateaus are observed starting at 2.3, 2.9, and 4.0 V. This correlation between charge

overpotential and discharge current density has also been observed for Li–O₂ cell.^{13–15}

To identify the nature of various charge plateaus, the NCNT-CP air electrodes were discharged to cutoff potential of 1.8 V at various current densities and then examined by XAS technique. XAS technique is chosen to analyze the chemical composition of the discharge product of the Na–O₂ cell since it exhibits both selectivity and sensitivity toward the various sodium oxide phases presented in the cell product. The normalized O K and Na K-edge XANES spectra of the NCNT-CP air electrodes discharged under different current densities along with a standard Na₂O₂ sample were recorded under the both surface sensitive total electron yield (TEY) and the bulk sensitive fluorescence yield (FLY) modes, as shown in Figure 3, panels b–e. All discharged electrodes, as well as the standard Na₂O₂ sample, exhibit a feature around 534.3 eV in the O K-edge XANES spectra (Figure 3b,d) relating to the excitation of the 1s electrons to empty 3σ_u (σ*) molecular orbital of Na₂O₂.^{33–35} Interestingly, a new feature at 532.9 eV appears when the discharge current density is increased from 0.1 to 0.5 and 1.0 mA cm⁻². This new feature, which increases in prominence with increased discharge current density, is related to the excitation of the 1s electrons to a semifilled 1π_g (π*) molecular orbitals of superoxide molecules.^{33–35} This same transition can also be seen in the case of standard Na₂O₂ sample, indicating the superoxide impurity phase of commercial Na₂O₂ sample (the pale yellow color of the commercial Na₂O₂ samples is a result of π_u–π_g transition in the superoxide ion).³⁶ These π* features are associated with unsaturated bonding occurring between oxygen in O₂ and O₂⁻. To confirm the existence of the superoxide phase (NaO₂) in the Na₂O₂ standard sample, the O K-edge XANES spectra of standard Li₂O₂, Na₂O₂, and KO₂ samples was also obtained (Figure S10). The standard Li₂O₂ sample displays a broad feature at around 532 eV, which is related to electron excitation into the σ* molecular orbitals. Furthermore, the KO₂ standard sample displays two features at around 533 and 534.5 eV related to 1s electron excitations to the π* and σ* molecular orbitals, respectively.^{33–35} The same superoxide characteristic feature (532.9 eV) also appears in the case of Na₂O₂ standard sample, which confirms the existence of superoxide impurity phase. It should also be noted that the small energy difference between σ* molecular orbitals of superoxide and peroxide phases cannot be distinguished here. However, a higher ratio of σ* to π* in the case of Na₂O₂ over KO₂ is probably a result of an overlap between the 1s electron excitations to the σ* molecular orbitals of superoxide and peroxide phases. Similar features can also be found in the O K-edge XANES spectra of the discharged electrodes recorded under the FLY mode (Figure 3d). The difference between chemical composition of surface and bulk components of the discharge products can be obtained by comparing of XANES spectra collected under TEY and FLY modes, respectively.⁸ Performing this comparison for discharged electrodes reveals that the bulk of the discharge product is predominantly composed of a superoxide-like phase. Reduced amount of superoxide-like phase at the external superficial layer of the discharge product is probably related to the side reaction between the highly oxidative superoxide phase of the discharge product and the electrolyte. Appearance of such a side product has not been observed in the previous studies involving the superoxide phase as the discharge product.^{3,22} However, occurrence of the side reaction can be rationalized considering the high surface area air electrode

employed in this study compared to the previous reports.^{3,22} Such a high surface area air electrode provides a vast interface between the discharge product and the electrolyte (see also Supporting Information, Figure S11 and 12), which results in formation of higher amount of side products. The nature of the side product in Na–O₂ cell will be more discussed in the following sections. It should also be mentioned that the difference between the spectra of the standard Na₂O₂ sample at around 534.3 eV recorded under the TEY and FLY modes is due to the different distribution of the two phases.

The XANES spectra for Na₂O₂ recorded in both TEY and FLY are also compared in a single plot in Figure S13. The corresponding Na K-edge XANES spectra recorded under the TEY and FLY modes are presented in Figure 3, panels c and e. The Na K spectra of discharged electrodes display the same oxidation state for atomic sodium as standard Na₂O₂. However, the intensity of the feature at around 1083 eV flattens out with increasing discharge current density, indicating increasing disorder in discharge products obtained at higher current densities, which is in accordance with XRD results (Figure S14).

NCNT-CP air electrodes were also subjected to restricted discharge capacity of 0.5 mAh cm⁻² and subsequently charged back to the charge plateaus of 2.75, 3.5, and 4.3 V, as displayed in Figure 3, panel f. The NCNT-CP air electrodes were then examined by XAS technique to identify the chemical composition of discharge product at each plateau. Normalized O and Na K-edge XANES spectra of NCNT-CP air electrodes charged to the various plateaus along with a standard Na₂O₂ sample recorded under the both TEY and FLY modes are depicted in Figure 3, panels g–j. The spectra of the discharged electrode are also added into the plot for the comparison purposes. After the air electrode was charged to 2.75 V, the feature associated with superoxide phase at 532.9 eV disappeared (Figure 3g,i), which indicates decomposition of the superoxide phase. The disappearance of the peak can be observed more obviously on the spectra recorded under the bulk-sensitive FLY mode (Figure 3i). Charging the NCNT-CP air electrode to 3.5 and 4.3 V reduces the feature at 534.3 eV, which indicates decomposition of the peroxide phase. Additionally, charging the electrode to 3.5 and 4.3 V also results in the appearance of another feature located at 533 eV, which can be correlated to the presence of a carbonate-like phase (see also Figure S15). It should also be noted that the features related to NaO₂ and Na₂CO₃ are very close. However, the feature at 532.9 eV disappears after the cell is charged to the cutoff voltage of 2.75 V, whereas Na₂CO₃ does not decompose under 4.0 V versus Na/Na⁺.¹⁸ Therefore, the feature at 532.9 eV that disappears when charging the cell to 2.75 V could not be related to the carbonate phase. The nature of the feature at 533 eV will be discussed more in the following section. Similar to the O K-edge, the Na K-edge also indicates the decomposition of products, as shown in Figure 3, panels h and j. However, no obvious changes can be detected between the Na K spectra of the discharged air electrode and the electrode charged back to 2.75 V. This may be due to the superoxide phase not showing any prominent peaks in the Na K spectra. However, the feature around 1078 eV significantly decreases when the electrode is charged to 3.5 and 4.3 V, which indicates decomposition of the peroxide phase during the second and third charge plateaus. The Na K-edge spectra of the NCNT-CP air electrode charged to 4.3 V are compared with standard Na₂O₂, Na₂CO₃, and NaSO₃CF₃ samples in Figure S16. XAS results suggest that a

carbonate-like phase is formed during the discharge cycle of the cell and decomposed during the third charging plateau. The formation of carbonate-based parasitic products on the carbonaceous air electrodes has also been observed for Li–air system.^{7,8,37} The formation of carbonate-based phase is discussed in the following section.

The NCNT-CP air electrode was also subjected to consecutive discharge and charge cycles restricted to capacities ranging from 0.14–1.0 mAh cm⁻² (Figure S17). The discharge and charge curves restricted to a capacity of 0.5 mAh cm⁻² cycled between 1.8 and 4.3 V under a current density of 0.1 mAh cm⁻² are depicted in Figure 4, panel a. Increasing cycle

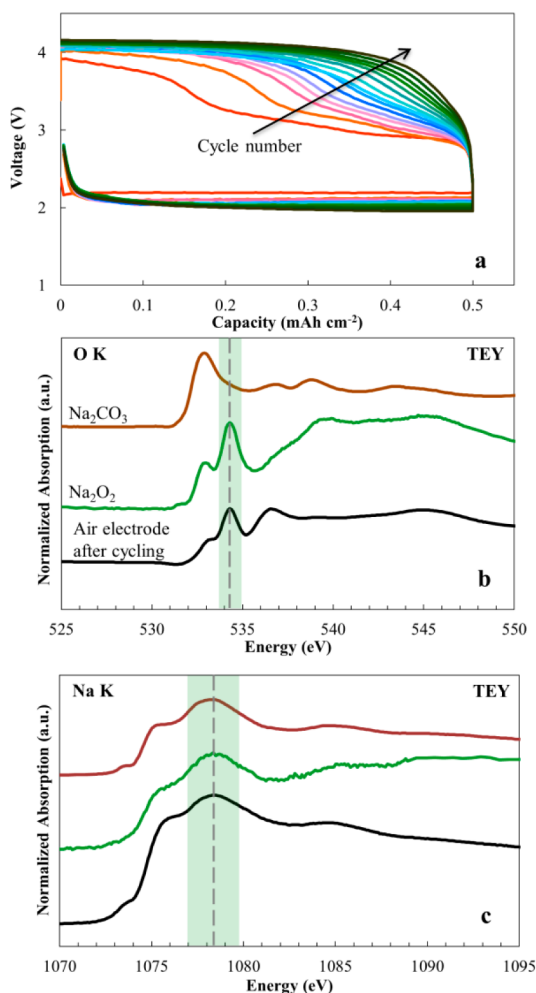


Figure 4. (a) Consecutive restricted discharge and charge curves of Na–O₂ cell using NCNT-CP air electrode cycled between 1.8 and 4.3 V at a current density of 0.1 mA cm⁻²; normalized (b) O and (c) Na K-edge XANES spectra recorded under the TEY mode for the cycled air electrode as well as the standard Na₂O₂ and Na₂CO₃ samples.

numbers lead to increased charge overpotential. While 70% of the formed product was charged back below 3.5 V during the first charge cycle, this value was decreased to 14% in the 15th cycle. To determine the nature of the remaining products after cycling, the NCNT-CP air electrodes were cycled in a Na–O₂ cell with a restricted capacity of 1.0 mAh cm⁻² under a current density of 0.1 mA cm⁻² and examined using XAS. The O and Na K-edge XANES spectra of the cycled air electrode as well as standard Na₂O₂ and Na₂CO₃ samples are presented in Figure 4, panels b and c. The comparison of the cycled air electrode with

the reference samples reveals that a carbonate-like phase as well as Na₂O₂ remains on the electrode after cycling. This insulating carbonate layer imposes an additional overpotential to the cell during the charge cycle and prevents complete decomposition of the discharge products.⁷ Such a gradual increase in the charging overpotential of the cell can also be seen in the consecutive discharge and charge curves shown in Figure 4, panel a. In addition, the cycled air electrodes restricted to different discharge capacities of 0.5 and 1.0 mAh cm⁻² were also examined by FTIR along with standard sodium peroxide and sodium carbonate samples (Figure S18). The FTIR results also confirm the existence of a carbonate phase on the cycled air electrodes.

Recently, McCloskey et al. compared the Li- and Na–O₂ cells using DEMS technique under similar experimental conditions and showed that unlike Li–O₂ cell, Na–O₂ undergoes less chemical and electrochemical decomposition during the first discharge/charge cycle.²² However, on basis of the XANES data presented here, it can be concluded that parasitic side products may also be produced and accumulated on the air electrode of Na–O₂ cell, especially when using a high surface area carbon material as the air electrode. High surface area air electrode provides a vast interface between the discharge products and the electrolyte, which results in the accelerated formation of the side products. Accumulation of the parasitic side products on the air electrode in turn results in increased cell overpotential and capacity fading.⁷ The Na–O₂ operational mechanism is schematically illustrated in Figure 5.

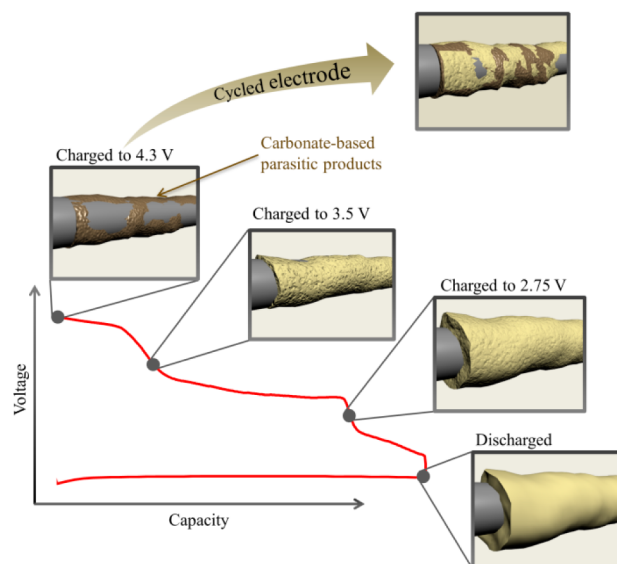


Figure 5. Schematic illustration of the Na–O₂ cell operational mechanism.

The source for the decomposition products is believed to mainly originate from the side reaction between the oxygen-rich phase of the discharge product (NaO₂) and the electrolyte.³⁸ Similar reaction mechanisms are expected to occur in Li–O₂ and Na–O₂ cells, and the formation of a superoxide intermediate is likely to occur for both cases.^{39,40} In Li–O₂ cells, the superoxide intermediate reacts with either the electrolyte or the carbonaceous air electrode to form Li₂CO₃ during the first discharge/charge cycle of the cell.^{7,8,38} In the case of Na–O₂ cells, however, higher thermodynamic stability of NaO₂ may contribute to decreased parasitic side reactions

occurring due to the stabilization of the superoxide intermediate. As a result, a lower amount of parasitic side products is expected to be formed in a Na–O₂ cell compared to Li–O₂ cells.

CONCLUSION

XANES study of the discharge products formed in Na–O₂ cell using a binder-free high surface area air electrode revealed that both sodium superoxide and peroxide are formed. Various sodium oxide phases formed during the discharge cycle of the cell exhibit dissimilar charging overpotentials. In addition, a parasitic side product with a carbonate-like structure was detected on the air electrode surface during the electrochemical cycling. It is believed that the quantity of the parasitic products in Na–O₂ cell is lower than that of Li–O₂ cell due to the higher thermodynamic stability of NaO₂ phase compared to LiO₂. However, the presence of carbonate parasitic side product cannot be ignored on a high surface area carbonaceous air electrode. Control of chemical composition of the discharge products in Na–O₂ cell either by manipulating the kinetic parameters affecting the discharge reaction or investigation for a more stable electrolyte might be considered as a potential solution in increasing the cyclability of Na–O₂ cells.

ASSOCIATED CONTENT

Supporting Information

Electrochemical response of the 3D air electrode, additional SEM micrographs, and extended characterization results including TGA, FTIR, XRD, and XAS. This material is available free of charge via the Internet at <http://pubs.acs.org>.

AUTHOR INFORMATION

Corresponding Author

*E-mail: xsun@eng.uwo.ca.

Notes

The authors declare no competing financial interest.

ACKNOWLEDGMENTS

This research was supported by Natural Sciences and Engineering Research Council of Canada, Canada Research Chair Program, Canada Foundation for Innovation, Canadian Light Source, and the University of Western Ontario.

REFERENCES

- (1) Bruce, P. G.; Freunberger, S. A.; Hardwick, L. J.; Tarascon, J. M. *Nat. Mater.* **2012**, *11*, 19–29.
- (2) Peng, Z.; Freunberger, S. A.; Chen, Y.; Bruce, P. G. *Science* **2012**, *337*, 563–566.
- (3) Hartmann, P.; Bender, C. L.; Vracar, M.; Dürr, A. K.; Garsuch, A.; Janek, J.; Adelhelm, P. *Nat. Mater.* **2013**, *12*, 228–232.
- (4) Girishkumar, G.; McCloskey, B.; Luntz, A. C.; Swanson, S.; Wilcke, W. *J. Phys. Chem. Lett.* **2010**, *1*, 2193–2203.
- (5) Kraysberg, A.; Ein-Eli, Y. *Nano Energy* **2013**, *2*, 468–480.
- (6) Kraysberg, A.; Ein-Eli, Y. *J. Power Sources* **2011**, *196*, 886–893.
- (7) McCloskey, B. D.; Speidel, A.; Scheffler, R.; Miller, D. C.; Viswanathan, V.; Hummelshøj, J. S.; Nørskov, J. K.; Luntz, A. C. *J. Phys. Chem. Lett.* **2012**, *3*, 997–1001.
- (8) Gallant, B. M.; Mitchell, R. R.; Kwabi, D. G.; Zhou, J.; Zuin, L.; Thompson, C. V.; Shao-Horn, Y. *J. Phys. Chem. C* **2012**, *116*, 20800–20805.
- (9) Ottakam Thotiyl, M. M.; Freunberger, S. A.; Peng, Z.; Chen, Y.; Liu, Z.; Bruce, P. G. *Nat. Mater.* **2013**, *12*, 1050–1056.

- (10) Lu, Y. C.; Gallant, B. M.; Kwabi, D. G.; Harding, J. R.; Mitchell, R. R.; Whittingham, S.; Shao-Horn, Y. *Energy Environ. Sci.* **2013**, *6*, 750–768.
- (11) Gallant, B. M.; Kwabi, D. G.; Mitchell, R. R.; Zhou, J.; Thompson, C. V.; Shao-Horn, Y. *Energy Environ. Sci.* **2013**, *6*, 2518–2528.
- (12) Yang, J.; Zhai, D.; Wang, H. H.; Lau, K. C.; Schlueter, J. A.; Du, P.; Myers, D. J.; Sun, Y. K.; Curtiss, L. A.; Amine, K. *Phys. Chem. Chem. Phys.* **2013**, *15*, 3764–3771.
- (13) Zhai, D.; Wang, H. H.; Yang, J.; Lau, K. C.; Li, K.; Amine, K.; Curtiss, L. A. *J. Am. Chem. Soc.* **2013**, *135*, 15364–15372.
- (14) Adams, B. D.; Radtke, C.; Black, R.; Trudeau, M. L.; Zaghbi, K.; Nazar, L. F. *Energy Environ. Sci.* **2013**, *6*, 1772–1778.
- (15) Zhai, D.; Wang, H. H.; Lau, K. C.; Gao, J.; Redfern, P. C.; Kang, F.; Li, B.; Indacochea, E.; Das, U.; Sun, H. H.; Sun, H. J.; Amine, K.; Curtiss, L. A. *J. Phys. Chem. Lett.* **2014**, *5*, 2705–2710.
- (16) Liu, W.; Sun, Q.; Yang, Y.; Xie, J. Y.; Fu, Z. W. *Chem. Commun.* **2013**, *49*, 1951–1953.
- (17) Li, Y.; Yadegari, H.; Li, X.; Banis, M. N.; Li, R.; Sun, X. *Chem. Commun.* **2013**, *49*, 11731–11733.
- (18) Kim, J.; Lim, H. D.; Gwon, H.; Kang, K. *Phys. Chem. Chem. Phys.* **2013**, *15*, 3623–3629.
- (19) Jian, Z.; Chen, Y.; Li, F.; Zhang, T.; Liu, C.; Zhou, H. *J. Power Sources* **2014**, *251*, 466–469.
- (20) Hartmann, P.; Bender, C. L.; Sann, J.; Katharina Dürr, A.; Jansen, M.; Janek, J.; Adelhelm, P. *Phys. Chem. Chem. Phys.* **2013**, *15*, 11661–11672.
- (21) Hartmann, P.; Grübl, D.; Sommer, H.; Janek, J.; Bessler, W. G.; Adelhelm, P. *J. Phys. Chem. C* **2014**, *118*, 1461–1471.
- (22) McCloskey, B. D.; Garcia, J. M.; Luntz, A. C. *J. Phys. Chem. Lett.* **2014**, *5*, 1230–1235.
- (23) Zhao, N.; Li, C.; Guo, X. *Phys. Chem. Chem. Phys.* **2014**, *16*, 15646–15652.
- (24) Lee, B.; Seo, D. H.; Lim, H. D.; Park, I.; Park, K. Y.; Kim, J.; Kang, K. *Chem. Mater.* **2014**, *26*, 1048–1055.
- (25) Kang, S.; Mo, Y.; Ong, S. P.; Ceder, G. *Nano Lett.* **2014**, *14*, 1016–1020.
- (26) Yadegari, H.; Li, Y.; Banis, M. N.; Lia, X.; Wang, B.; Sun, Q.; Li, R.; Sham, T. K.; Cui, X.; Sun, X. *Energy Environ. Sci.* **2014**, *7*, 3747–3757.
- (27) Liu, J.; Zhang, Y.; Ionescu, M. I.; Li, R.; Sun, X. *Appl. Surf. Sci.* **2011**, *257*, 7837–7844.
- (28) Gong, K.; Du, F.; Xia, Z.; Durstock, M.; Dai, L. *Science* **2009**, *323*, 760–764.
- (29) Geng, D.; Chen, Y.; Chen, Y.; Li, Y.; Li, R.; Sun, X.; Ye, S.; Knights, S. *Energy Environ. Sci.* **2011**, *4* (2011), 760–764.
- (30) Li, Y.; Wang, J.; Li, X.; Liu, J.; Geng, D.; Yang, J.; Li, R.; Sun, X. *Electrochem. Commun.* **2011**, *13*, 668–672.
- (31) Li, Y.; Yadegari, H.; Li, X.; Banis, M. N.; Li, R.; Sun, X. *Chem. Commun.* **2013**, *49*, 11731–11733.
- (32) Sun, Q.; Yadegari, H.; Banis, M. N.; Liu, J.; Xiao, B.; Wang, B.; Lawes, S.; Li, X.; Li, R.; Sun, X. *Nano Energy* **2015**, *12*, 698–708.
- (33) Puglia, C.; Bennich, P.; Hasselstrom, J.; BrOhwiler, P. A.; Nilsson, A.; Maxwell, A. J.; Martensson, N.; Rudolf, P. *Surf. Sci.* **1997**, *383*, 149–161.
- (34) Puglia, C.; Bennich, P.; Hasselstrom, J.; BrOhwiler, P. A.; Nilsson, A.; Li, Z. Y.; Rudolf, P.; Martensson, N. *Surf. Sci.* **2001**, *488*, 1–6.
- (35) Hrbek, J.; Sham, T. K.; Shek, M. L.; Xu, G. Q. *Langmuir* **1992**, *8*, 2461–2472.
- (36) Creighton, J. A.; Lippincott, E. R. *J. Chem. Phys.* **1964**, *40*, 1779–1780.
- (37) Ottakam Thotiyl, M. M.; Freunberger, S. A.; Peng, Z.; Bruce, P. G. *J. Am. Chem. Soc.* **2013**, *135*, 494–500.
- (38) McCloskey, B. D.; Valery, A.; Luntz, A. C.; Gowda, S. R.; Wallraff, G. M.; Garcia, J. M.; Mori, T.; Krupp, L. E. *J. Phys. Chem. Lett.* **2013**, *4*, 2989–2993.

(39) Peng, Z.; Freunberger, S. A.; Hardwick, L. J.; Chen, Y.; Giordani, V.; Bardé, F.; Novák, P.; Graham, D.; Tarascon, J. M.; Bruce, P. G. *Angew. Chem., Int. Ed.* **2011**, *123*, 6475–6479.

(40) Freunberger, S. A.; Chen, Y.; Drewett, N. E.; Hardwick, L. J.; Barde, F.; Bruce, P. G. *Angew. Chem., Int. Ed.* **2011**, *50*, 8609–8613.